Analytical Heat Transfer Model for Laterally Perforated-FinnedHeat Sinks

Mohammad Reza Shaeri*, Richard W. Bonner III

Advanced Cooling Technologies, Inc., Lancaster, PA 17601

Abstract

An analytical model isproposed to predict the average Nusselt numbers of laterally perforated-finned heat sinks (LA-PFHSs) with high aspect ratios in forced convection laminar flows. The model is developed based on the experimental data acquired from testing air-cooled heat sinks including square cross-sectional perforations distributed equidistantly along the length of the fins. The experiments were conducted using three different perforation sizes and five different porosities at each perforation size. The accuracy of the experiments was validated by comparing the experimental pressure drops and heat transfer coefficients of the heat sink without perforation with those obtained from thewidely acceptedcorrelations in the literature.Thedeveloped model in this study predicts the Nusselt number as a function of Reynolds number, Prandtl number, fin and perforation geometrical parameters, porosity, and the distances between perforations. The model showed excellent predictions for the Nusselt numbers of all LA-PFHSs tested in this study to be within$\pm 12\%$of the experimental dataand a mean absolute error of4.90%. This study is the first attempt in the literature to develop an analytical model based on experimental data for investigating heat transfer in LA-PFHSs.

Keywords: Air-cooled heat sink; Perforated fin; Boundary layer interruption; Analytical model; Nusselt number.

*Corresponding author.

E-mail: mohammadreza.shaeri@1-act.com; oveisshaeri@gmail.com

Telephone: +1-717-205-0653

Nomenclature

A_S : Area of an individual section in azone (m^2)

A_{th} : Heat transfer area inside a channel(m^2)

d : Distance between the plane of the embedded thermocouples and the fin/channel base (m)

D_h : Channel hydraulic diameter (m)

f : Friction factor

f_{app} : Apparent friction factor

h : Average heat transfer coefficient (W/m^2.K)

H : Channel height (m)

H_{ed} : Distances between the lowest row of perforationsand the fin base, and that between the top row of perforations and the fin tip (m)

H_S : Height of an individual section in a zone (m)

K_f : Air thermal conductivity (W/m.K)

K_c : Sudden contraction loss

K_e : Sudden expansion loss

K_s : Thermal conductivity of the heat sink (W/m.K)

L : Channel length (m)

L_p : Perforation length (m)

L_S : Length of an individual section in a zone (m)

L_{LB} : The equivalent length to the lower bound thermal performance of a section in zone 3

L_{UB} : The equivalent length to the upper bound thermal performance of a section in zone 3

MAE : Mean absolute error

N : Number of channels

N_C : Number of perforation columns

N_P : Number of perforations

N_R : Number of perforation rows

N_S : Number of sections in a zone

Nu_{ex} : Experimental Nusselt number

Nu_{LB} : Nusselt number of a section in zone 3 based on the lower bound thermal performance assumption

Nu_{UB} : Nusselt number of a section in zone 3 based on the upper bound thermal performance assumption

$Nu_{pr,LA\text{-}PFHS}$: Predicted Nusselt numberof LA-PFHSs

$Nu_{pr,SFHS}$: Predicted Nusselt numberof SFHS

Nu_S : Nusselt number of an individual section in a zone

P_p : Pumping power (W)

Pr : Prandtl number

ΔP : Pressure drop across the heat sink (Pa)

Q_{input} : Electrical input heat (W)

Re : Reynolds number

Ri : Richardson number

S_x : Horizontal distance between adjacent perforations (m)

S_y : Vertical distance between adjacent perforations (m)

t_b : Heat sink base thickness (m)

t_f : Fin thickness (m)

T_b : Local heat sink base temperature (K)

$T_{b,max}$: Maximum local temperature at heat sink base (K)

T_{film} : Film temperature (K)

T_i : Inlet air temperature (K)

T_o : Outlet air temperature (K)

$T_{s,avg}$: Average fin/channel base temperature (K)

U : Approach velocity (m/s)

$\dot{V}_{ch}$: Volume flowrate inside the channel (m^3/s)

$\dot{V}_t$: Volume flowrate inside the duct (m^3/s)

W : Heat sink width (m)

W_{ch} : Channel width (m)

x^+ : Dimensionless hydrodynamic length

Greek symbols

α: Either the aspect ratio or the inverse of the aspect ratio of the channel, whichever that is less than unity

β: Weighting function

ε: Frontal-area ratio

μ: Dynamic viscosity (Pa.s)

ρ: Air density (kg/m^3)

ϕ: Porosity

ψ: Deviation of the predicted Nusselt numbers from the experimental Nusselt numbers

1. Introduction

Air-cooled heat sinks have been widely used as primary thermal management solutions in a broad range of applications due to their simplicity, reliability, low cost, and ease of maintenance [1].These cooling systems consist of fans to blow air through parallel channels that are separated from each other via fins. Attached to heat sinks are heat sources that are cooled by exchanging heat to the flowing air inside the channel.However, mainly due to poor thermal properties of the air as the coolant, low heat transfer coefficientsare the serious drawbacks of air-cooled heat sinks. Overcoming theselimitationsby increasing the air velocity is not practically acceptable because the airflow is usually laminar or weakly turbulent in air-cooled heat sinks due to constraints in space and pumping power [2]. As a result, enhancement of heat transfer in air-cooled heat sinks through practically acceptable techniques has been the subject of extensive research.

Theoretically, any technique to interruptthe boundary layer in order to hinder its further growth over a heating surface leads to enhance the heat transfer [3].One of the popular related techniques is using perforated fins, which also offers another advantage as more lightweight heat sinks due to perforations. The most conventional categories of perforated fins are longitudinally and laterally perforated fins such that the first category encompasses perforations along the length of the fins [4-7], and the second category includes perforations on the lateral sides of the fins [8-16].However, while an increase in the heat transfer area is the major reason to enhanceheat transfer in a longitudinally perforated fin, heat transfer enhancement in a laterally perforated fin is due to the boundary layer interruption such that the boundary layer is frequently terminated and restarted before and after the perforations, respectively. Moreover, from the practical point of view, fabrication of laterally perforated fins is much simpler and more economical compared with that of longitudinally perforated fins because most fins that are used in industrial applications are thin with relatively high aspect ratios.Therefore, laterally perforated fins are the subject

of the present study. Aheat sink made by these types of fins is called laterally perforated-finned heat sink (LA-PFHS).

An accurate prediction of heat transfer coefficients of a heat exchanger is crucial to reduce the cost of design and avoid the drastic results due to underdesign or overdesign of the heat exchanger [17, 18]. However, such accurate prediction requires a sufficient understanding of the physics of the fluid flow and heat transfer in the heat exchanger. Despite relatively well-documented and accurate correlations to describe heat transfer coefficients and pressure drops in a solid-finned heat sink (SFHS, a heat sink without perforations), such knowledge is still limited in LA-PFHSs. This limitation is mainly due to the complex physics of fluid flow resulting from the frequent boundary layer interruptions along with the flow interactions over the perforations with each other, as well as the lack of detailed and fundamental research to address those complex phenomena. The computational works by the present author in [8, 9] were among the first comprehensive studies to illustrate the flow structures over rectangular cross-sectional perforations in LA-PFHSs covering a broad range of perforation sizes and porosities in both turbulent and laminar flows. In addition, the effects of perforations on the individual drag components (friction and pressure drags) as well as the temperature distributions across the surface of the fins were investigated in those studies. In conclusion, correlations were developed to predict the average Nusselt number as a function of both Reynolds number and porosity. However, those correlations are not physics-based and were developed by curve-fitting of the computational results.The study by Shaeri et al. [8] was extended by other researchers. Ismail et al. [10] repeated the study in [8] by changing the geometry of perforations from square to circular, hexagonal, and triangular cross sections, through a computational research. Willockx [11] extended the study in [8] by applying the inverse heat conduction problem technique to fins with one and two lateral perforations, and confirmed the results obtained in [8] about the thinning of the boundary layer due to a negative pressure gradient in the perforation.Dhanawade et al. [12, 13] and Al-Doori [14] investigated the thermal performances of LA-PFHSs and reported enhancement in heat transfer by relying on the open area of the fins, which includes the surfaces inside the perforations as well.However, in our recent studies in [15, 16], it was demonstrated that comparison of heat transfer coefficients of LA-PFHSs based on their open areas leads to under/overestimated thermal performances due to a monotonic change in the open area by increasing the porosity. Also, there are several studies about thermal performances of heat exchangers including laterally perforated finslocated on tubes, not parallel plate-finned heat sinks[19-22].However, due to frequent interruptionsof the boundary layer along the surfaces of relatively long fins in LA-PFHSs, the thermo-fluid physics in LA-PFHSs could be different from that in the perforated fins used in the heat exchangers investigated in [19-22].

Recently, the authors demonstrated the capability of LA-PFHSs to enhance cooling performances without any penalty in pumping power, through a series of experiments [15, 16, 23]. In our recent work in [15],

the thermal and hydraulic performances of LA-PFHSs operating in the laminar flow regime were investigated for a broad range of perforation sizes and porosities. In addition, the study in [15] presented the first published experimental local thermal characteristics of LA-PFHSs. Through our other recent studies in [16, 23], the pressure drops and heat transfer from LA-PFHSs across a wide range of flow regimes ranging from laminar to turbulent flows were investigated. The dominance of the pressure dragcompared with the friction drag in LA-PFHSs was demonstrated in [15, 16, 23]. Also, by defining three different parameters in [15, 16, 23], the merits of LA-PFHSs were classified into three industrial demands that require (i) colder heat sinks to dissipate a fixed amount ofheat, (ii) more uniform temperature on the heat sink bases, and (iii)more lightweight heat sinks.These categories signify that designing an efficient LA-PFHS highly depends on the design goal.

Precise physics-based correlations to describe heat transfer in LA-PFHSs based on the key elements such as geometrical parameters and flow conditions help better understanding the thermo-fluid physics of LA-PFHSs, optimization of LA-PFHSs by change in design parameters, reducing the overall cost ofLA-PFHSsby avoiding try and error to find the optimized heat sinks, and ultimately commercialization of LA-PFHSs.The present study is a supplement to our recent experimental research in [15] to develop a physics-based correlation to predict Nusselt numbers of LA-PFHSs in laminar forced convection flows. This study is the first attempt in the literature to propose physics-based correlations based on experimental data.

2. Experiment

2.1. Experimental setup

Fig. 1 illustrates the CAD model of the experimental setup and its exploded view. The airflow was provided by a centrifugal blower (RG90-18/12N, ebm-papst Inc.) through a 91 cm long stainless steel duct with a rectangular cross section of 7.3 cm by 4.3 cm. The air velocities inside the duct were adjusted by regulating voltages of a DC power supply that powered the blower. The inlet and outlet air temperatures were measured using two resistance temperature detector (RTD) probes (PR-26A-3-100-A-1/8-0600-M12-1, OMEGA Engineering, Inc.) that were inserted at the entrance and exit of the heat sink, respectively. The pressure drop across the heat sink was measured by a differential pressure transducer (PX653-01D5V, OMEGA Engineering,Inc.).A transparent polycarbonate cover formed the top surface of the duct. The duct was completely airtight by placing an adhesive neoprene rubber gasket between the duct flange and the polycarbonate cover, which was clamped in place between the cover and the flange. Fig. 2(a) illustrates the CAD model of a LA-PFHS with two rows of perforations. Heat sinks were made of 6063-T5 aluminum alloy and included 19 parallel channels (20 fins) with the fin thickness at 0.96 mm, and the channel length, height, and width at 203 mm, 22.86 mm, and 2.18 mm, respectively. The

thickness of the heat sink base was at 2.54 mm. Perforations with square cross sections were fabricated on the lateral surfaces of the fins through the electrical discharge machining technique. Totally, 16 heat sinks were used for conducting the experiments. Table 1 summarizes the parameters of the heat sinks used in this study. The SFHS (shown as Solid in Table 1) wasused as the base for comparisons. Each LA-PFHS is recognized by two numbers, as the first number represents the porosity, and the second number inside the parenthesis as the perforation size in mm. The porosity is defined as the ratio of void volume of the fin due to perforations, to the volume of the solid fin (without perforations), as follows:

$$\phi = \frac{N_P L_P^2}{HL} \tag{1}$$

The experiments were performed for five different porosities at 0.15, 0.25, 0.35, 0.45, and 0.55.Each porosity was investigated under three perforation sizes of 5.08 mm, 7.62 mm, and 15.24 mm.

Table 1. Geometrical information of the perforations associated with the different heat sinks in this study.

Heat sink	N_P	L_P (mm)	S_x (mm)	S_y (mm)	N_R	ϕ(porosity)
Solid	0	n/a	n/a	n/a	n/a	0
0.15 (5.08)	27	5.08	15.75	1.91	3	0.15
0.15 (7.62)	12	7.62	25.4	2.54	2	0.15
0.15 (15.24)	3	15.24	39.37	n/a	1	0.15
0.25 (5.08)	45	5.08	7.87	1.91	3	0.25
0.25 (7.62)	20	7.62	11.43	2.54	2	0.25
0.25 (15.24)	5	15.24	20.32	n/a	1	0.25
0.35 (5.08)	63	5.08	4.32	1.91	3	0.35
0.35 (7.62)	28	7.62	6.35	2.54	2	0.35
0.35 (15.24)	7	15.24	12.07	n/a	1	0.35
0.45 (5.08)	81	5.08	2.34	1.91	3	0.45
0.45 (7.62)	36	7.62	3.56	2.54	2	0.45
0.45 (15.24)	9	15.24	6.60	n/a	1	0.45
0.55 (5.08)	99	5.08	1.04	1.91	3	0.55
0.55 (7.62)	44	7.62	1.52	2.54	2	0.55
0.55 (15.24)	11	15.24	2.95	n/a	1	0.55

As shown in Fig. 2(b), five grooves at different distances from the inlet of the heat sink were machined on the heat sink base. Five T-type thermocouples (TJC36-CPSS-032G-12, OMEGA Engineering,Inc.) were placed in these grooves, and the spaces between the thermocouples and the grooves were filled with a

bonding resin.A $51\ \text{mm} \times 203\ \text{mm}$ insulated flexible heater (KH-208/10-P, OMEGA Engineering, Inc.) that had almost the same footprint as that of the heat sink base was glued on the heat sink base, and provided a uniform heat load to the base. The heater was powered by a variable transformer (3PN116C, 0-140 V, 10 A, Superior Electric). A multi-meter (FLUKE 117 TRUE RMS) and a clamp meter (FLUKE 376 TRUERMS) were used to measure the supplied voltage and current to the heater, respectively. The heat loss to the ambient was minimized by covering the floor of the duct, and all other sides of the heat sinksby thermal insulation layers. Signals from the thermocouples, RTD probes, and differential pressure transducer were collected by a Keithley 2700 data acquisition system.

An individual test included measuring the data at a specific input blower voltage and an input electrical heat. The data was collected for three minutes of operation after reaching a steady state condition. Steady state was considered to be reached when the changes in the temperatures obtained by RTD probes as well as individual embedded thermocouples in the heat sink base were below $0.2\ ^{\circ}\text{C}$ over 10minutes of operation. The experiments were proceeded by increasing the input blower voltage from 8 V to 14 V by increments in 1 V at a fixed input heat load.This process was repeated until all the input blower voltages and input heat loads were tested for all heat sinks. The experiments were conducted at two heat inputs of 50 W and 100 W. Also, the excellent repeats of experimental results were obtained for over three months. An airflow bench was used to determine the airflow rates inside the ductby obtaining the actual operating point of an individual heat sink subject to an individual blower voltage. Then, the volume flow rate, approach velocity,and Reynolds number associated with an individual channel, as well as the pumping power are calculated as follows:

$$\dot{V}_{\text{ch}} = \frac{\dot{V}_t}{N} \tag{2}$$

$$U = \frac{\dot{V}_{\text{ch}}}{W_{\text{ch}} H} \tag{3}$$

$$\text{Re} = \frac{\rho U D_h}{\mu} \tag{4}$$

$$P_p = \dot{V}_t \times \Delta P \tag{5}$$

where

$$D_h = \frac{2HW_{\text{ch}}}{H + W_{\text{ch}}} \tag{6}$$

2.2. Data reduction

The heat loss $\left(Q_{\text{loss}}\right)$ from the heat sink to the ambient is calculated by subtracting the sensible absorbed heat by the air $\left(Q_{\text{conv}}\right)$ from the electrical input heat $\left(Q_{\text{input}}\right)$ as follows:

$$Q_{\text{loss}} = Q_{\text{input}} - Q_{\text{conv}} = I \times V - \left[\rho \dot{V}_t c_p \left(T_o - T_i\right)\right] \tag{7}$$

where *I* and *V* are the current and voltage, respectively, provided by the variable transformer to the heater. Due to the low heat loss in the present experiments, ranged from 4.2-9.3%, it is assumed that the whole input heat was absorbed by the heat sink; therefore, Q_{input} was used for the data reduction.

The average heat transfer coefficient is correlated as follows:

$$h = \frac{\left(\frac{Q_{\text{input}}}{N}\right)}{A_{\text{ch}}\left(T_{s,\text{avg}} - T_i\right)} \tag{8}$$

where $\frac{Q_{\text{input}}}{N}$ stands for the heat input to an individual channel.Due to using fins with a high aspect ratio in the present experiments $\left(H \gg W_{\text{ch}}\right)$, the heat transfer area inside an individual channel ofeach heat sinkis described as follows:

$$A_{\text{ch}} = 2HL\left(1-\phi\right) \tag{9}$$

which for $\phi = 0$,it corresponds to the heat transfer area inside the channels of a high aspect ratio SFHS [24]. Heat sinks made by high aspect ratio fins are the most popular heat sinks in power electronics applications since they provide a larger fin density for a given footprint, which results in a greater surface area for maximum heat dissipation[24].

The average channel base temperature is calculated by assuming one-dimensional heat diffusion in a distance *d*, which is the distance between the plane of the embedded thermocouple and the channel base [25]:

$$T_{s,\text{avg}} = \frac{\sum_{i=1}^{5} T_{b,i}}{5} - \frac{Q_{\text{input}} d}{K_s LW} \tag{10}$$

where the number 5 corresponds to the number of embedded thermocouples in the heat sink base.

In this study, the average heat transfer coefficient is non-dimensionalized by the average Nusselt number and expressed as follows [24, 26]:

$$Nu_{ex} = \frac{hW_{ch}}{K_f} = \frac{\left(\frac{Q_{input}}{N}\right)W_{ch}}{K_f\left(2HL\right)\left(1-\phi\right)\left(T_{s,avg}-T_i\right)} \tag{11}$$

All the air properties at this study were calculated at the film temperature, unless otherwise is stated:

$$T_{film} = \frac{T_i + T_{s,avg}}{2} \tag{12}$$

2.3. Uncertainty analysis

The uncertainties of the instruments used in the present experiments were based on the information provided by their manufacturers. The uncertainty of T-type thermocouples, differential pressure transducer, dimensions, airflow bench, variable transformer, and RTD probeswas at $\pm 0.5℃$, 0.3% of full scale, $\pm\ 2.54\times10^{-2}$ mm, $\pm 2\%$ of the measured flow rate, $\pm 2\%$ of the voltage, and $\pm\left(0.15+0.002t\right)℃$ with *t* as the temperature in $^\circ$C, respectively. The uncertainty of the property*R*that is a function of variables X_1, X_2, …, X_i, is calculated as follows [27-29]:

$$\delta R = \left[\sum_{i=1}^{N}\left(\frac{\partial R}{\partial X_i}\delta X_i\right)^2\right]^{\frac{1}{2}} \tag{13}$$

where δX_i corresponds to the uncertainty of the *i*th measured value. Therefore, the maximum uncertainty of Q_{input}, Re, U, P_p, $T_{s,avg}$, and Nu_{ex} was below 2.00%, 2.55%, 2.32%, 2.46%, 0.56%, and 2.87%, respectively.

3. Validation of experiment

To assess the effect of natural convection heat transfer, the Richardson numberas the ratio of the Grashof number to the square of the Reynolds number based on the fin height was calculated for all the heat sinks as follows [30, 31]:

$$\mathrm{Ri} = \frac{\mathrm{g}H\left(\frac{1}{\frac{T_i+T_{s,avg}}{2}+273.15}\right)\left(T_{b,max}-T_i\right)}{U^2} \tag{14}$$

where g is the gravitational acceleration, and the first and second terms inside the parentheses correspond the thermal expansion coefficient, and the maximum temperature difference in the experiment, respectively. Since the maximum Richardson numberfor the operating conditions in this study was below 0.003 (much less than unity), the forced convection was the dominant mode of heat transfer [30, 31].

The accuracy of the present experiment is assessed by comparing the experimental pressure drops and Nusselt numbers of the SFHS against those obtained from widely accepted correlations in the literature.The pressure drop across a SFHS is described as follows [32, 33]:

$$\Delta P = \frac{\rho U^2}{2}\left[K_c + K_e + 4x^+ f_{\text{app}}\,\text{Re}\right] \tag{15}$$

where the apparent friction factor, dimensionless hydrodynamic length, sudden contraction loss, sudden expansion loss, and frontal-area ratio are described as follows:

$$f_{\text{app}}\,\text{Re} = \left[\left(\frac{3.44}{\sqrt{x^+}}\right)^2 + \left(f\,\text{Re}\right)^2\right]^{0.5} \tag{16}$$

$$x^+ = \frac{L}{D_h\,\text{Re}} \tag{17}$$

$$K_c = 0.42\left(1-\varepsilon\right) \tag{18}$$

$$K_e = \left(1-\varepsilon\right)^2 \tag{19}$$

$$\varepsilon = \frac{NW_{\text{ch}}H}{\text{duct cross sectional area}} \tag{20}$$

Also, the Poiseuille number for a laminar flow in a rectangular duct is calculated as shown below [34]:

$$f\,\text{Re} = 24\left(1-1.3553\alpha+1.9467\alpha^2-1.7012\alpha^3+0.9564\alpha^4-0.2537\alpha^5\right) \tag{21}$$

where α is either the aspect ratio or the inverse of the aspect ratio of the channel, whichever that is less than unity.

For calculating the Nusselt number in a SFHS, Teertstra et al. [24, 26] proposed the following correlation that was validated by experiments:

$$Nu_{\text{pr,SFHS}} = \frac{\tanh\sqrt{2Nu_i\dfrac{K_f H^2}{K_s W_{\text{ch}} t_f}\left(\dfrac{t_f}{L}+1\right)}}{\sqrt{2Nu_i\dfrac{K_f H^2}{K_s W_{\text{ch}} t_f}\left(\dfrac{t_f}{L}+1\right)}}Nu_i \tag{22}$$

where

$$Nu_i = \left[\frac{1}{\left(\frac{\mathrm{Re}_b^* \mathrm{Pr}}{2} \right)^3} + \frac{1}{\left(0.664 \sqrt{\mathrm{Re}_b^*}\, \mathrm{Pr}^{1/3} \sqrt{1 + \frac{3.65}{\sqrt{\mathrm{Re}_b^*}}} \right)^3} \right]^{-1/3} \quad (23)$$

$$\mathrm{Re}_b^* = \frac{\rho U W_{\mathrm{ch}}}{\mu} \times \frac{W_{\mathrm{ch}}}{L} \quad (24)$$

Also, the experimental Nusselt number in the study by Teertstra et al. [24, 26] was calculated from Eq (11) by inserting $\phi = 0$. The comparisons between experimental and correlated values in this study are illustrated in Fig. 3. The maximumdifference between experimental and correlated pressuredrops, and that between the experimental and correlated Nusseltnumbers are below 9.4%, and 8.0%, respectively, which indicate the good accuracy of the present experiments.

4. Model development

4.1. Problem description

The objective of this study is to develop an analytical model for predicting the average Nusselt numbers of high aspect ratio LA-PFHSsin forced convection laminar flows. The model is developed based on the experimental data obtained from testing heat sinks whose geometrical information is provided in section 2.1 and Table 1.The perforations with square cross sections are inserted equidistantly in an inline configuration on the lateral surfaces of the fins.

First, a fin is divided into several sections. Althoughthe number of sectionsmay be different in various LA-PFHSs, all sections fall into one of the three major zones as described below and schematically shown in Fig. 4:

- Zone 1: This zone includes two sections; one section corresponds to the area between the lowest row of perforations and the fin base, and another section is the area between the top row of perforations and the fin tip.The corresponding length, height, and area of each section in this zone are as follows:

$$L_{\mathrm{S},1} = L \quad (25)$$

$$H_{\mathrm{S},1} = H_{\mathrm{ed}} \quad (26)$$

$$A_{\mathrm{S},1} = H_{\mathrm{ed}} \times L \quad (27)$$

- Zone 2: This zone includes the sections between each two adjacent perforation rows.There are $N_R - 1$ sections in this zone; therefore, there is not any section in this zone for LA-PFHSs with the largest-sized perforations (15.24 mm) in the present experiments because $N_R = 1$ in theses heat sinks. The corresponding length, height, and area of each section in this zone are as follows:

$$L_{\mathrm{S},2} = L \tag{28}$$

$$H_{\mathrm{S},2} = S_y \tag{29}$$

$$A_{\mathrm{S},2} = S_y \times L \tag{30}$$

- Zone 3: This zone includes the sections that cover perforation rows; therefore, there are N_R sections in this zone. The corresponding length, height, and area of each section in this zone are as follows:

$$L_{\mathrm{S},3} = L - \left(N_{\mathrm{C}} \times L_P\right) \tag{31}$$

$$H_{\mathrm{S},3} = L_P \tag{32}$$

$$A_{\mathrm{S},3} = \left(L_P \times L\right) - \left(N_{\mathrm{C}} \times L_P^2\right) \tag{33}$$

Then, the predicted Nusselt number of a LA-PFHS is calculated by an area-weighted average technique as follows:

$$Nu_{\mathrm{pr,LA\text{-}PFHS}} = \frac{\sum_{i=1}^{3} N_{\mathrm{S},i} A_{\mathrm{S},i} Nu_{\mathrm{S},i}}{\sum_{i=1}^{3} N_{\mathrm{S},i} A_{\mathrm{S},i}} \tag{34}$$

where N_{S} stands for the number of sections in a zone, Nu_{S} is the Nusselt number of an individual section in a zone, and index *i* corresponds to the *i*th zone.

The methods of calculating the Nusselt numbers in different zonesare described in the next sections.

4.2. Nusselt numbers ofzones 1 and 2

Since there is not any perforation in the sections of zones 1 and 2, each section can be considered as a solid fin with geometrical information described by Eqs (25) to (27) for sections in zone 1, and Eqs (28) to (30) for sections in zone 2. Then, the Nusselt number of each section is calculated from Eqs (22) to (24) by using the corresponding length and height of each section.

4.3. Nusselt number ofzone3

The complexphysics of fluid flow and heat transfer ina perforated fin is resulting from flow patterns over perforations that are located in zone 3. Therefore, a precise prediction of Nusselt number of a LA-PFHS strongly depends on using an accurate technique to model heat transfer in zone 3.However, instead of relatively well-understood thermo-fluid physics and well-documented correlations to describe heat transfer in SFHSs, such knowledge is still limited in LA-PFHSs. Therefore, as long as a detailed understanding of the complex thermo-fluid physics in LA-PFHSs is not available, developing a generalized model to predict Nusselt number of a LA-PFHS as a function of key parameters such as fin geometry, perforation size, number of perforations, distance between perforations, etc., is challenging. For this reason, prediction of Nusselt numbers of LA-PFHSs in this study is performed through a simplified model. The logic behind the proposed model in this study is that the thermal performance of a LA-PFHS falls between the upper and lower bound thermal performances, similar to the simplified technique used by Teertstra et al. [26] for predicting the Nusselt numbers of slotted-finned heat sinks. Slotted-finned heat sinks consist of slots with the same sizes and spaces that are cut into the fins from the fin tip to the baseplate [26].The reason of using the same technique proposed in [26] for predicting the Nusselt numbers of LA-PFHSs in the present study is the similar concept of frequent boundary layer interruptions due to both slots and perforations. The upper and lower bound thermal performances are described in the following sections.

4.3.1. Nusselt number based on the upper bound thermal performance

The frequent terminating and restarting the boundary layer before and after perforations, respectively, is the first implication of using perforated fins. Therefore, the highest theoretical thermal performance of a perforated fin is obtained when the boundary layer is formed and terminated in the distance between two adjacent perforations, independent of any upstream effects. This indicates that the equivalent length to the upper bound thermal performance is as follows:

$$L_{\mathrm{UB}} = S_x \tag{35}$$

Then, the Nusselt number based on the upper bound thermal performance of a section in zone 3 is calculated from Eqs (22) to (24) by using L_{UB} and $H_{\mathrm{S,3}}$ as the length and height, respectively.

4.3.2. Nusselt number based on the lower bound thermal performance

The lower bound thermal performance of a section in zone 3 corresponds to when no new thermal boundary layers are formed over the surfaces of the fins. Therefore, the equivalent length to the lower

bound thermal performance is obtained by combining the length of all solid parts in a given section, as follows:

$$L_{\mathrm{LB}} = L - \left(N_C \times L_P \right) \tag{36}$$

which is equal to the length of each section in zone 3, described by Eq (31). Then, the Nusselt number based on the lower bound thermal performance of a section in zone 3 is calculated from Eqs (22) to (24) by using L_{LB} and $H_{\mathrm{S,3}}$ as the length and height, respectively.

5. Results and discussion

Since the thermal performances as well as the pressure drops associated with the LA-PFHSs tested in the present experiments were comprehensively discussed in our recent published work in [15], they are omitted in thisstudy. The present study is a supplement to our recent work in [15] by predicting the Nusselt numbers of LA-PFHSs.

The deviation of predicted Nusselt numbers from their corresponding experimental valuesis obtained as follows:

$$\psi = \frac{Nu_{\mathrm{pr,LA\text{-}PFHS}} - Nu_{\mathrm{ex}}}{Nu_{\mathrm{ex}}} \times 100 \tag{37}$$

Therefore, a negative and positive value of ψ corresponds to underpredicted and overpredicted Nusselt numbers, respectively.The experimental Nusselt numbers are calculated from Eq (11).

5.1. The effects of upper bound and lower bound thermal performances

Fig. 5 illustrates the predicted Nusselt numbers of all LA-PFHSs tested in the present experiments. The data associated with an individual perforation size cover the entire range of Reynolds numbers and porosities in this study. The predicted Nusselt numbers were calculated from Eq (34) while the Nusselt number of zone 3 was calculated based on the upper bound thermal performance assumption for the sections in this zone. The significantly overpredicted Nusselt numbers indicate thatconsidering only the boundary layer interruption, independent of any upstream effects, is not an accurate assumption for predicting Nusselt numbers of LA-PFHSs. In the recent study by the authors in [3], it was demonstrated that flow interactions over the perforations with each other are one of the key mechanisms affecting thermo-fluid physics in LA-PFHSs. This mechanismhighly depends on the Reynolds number, the distance between adjacent perforations, and the number of perforation rows.For a better understanding, flow pathlines inside and over perforationsfor two different LA-PFHSs with different porosities, number of perforations, distances between perforations, and number of perforation rowsare illustrated in Fig. 6, based on the previous work by the authorin [9].

Another finding from Fig. 5 is an increase in both the upper and lower bound deviations by a monotonic decrease in the perforation size such that $+68\% < \psi < +19\%$, $+91\% < \psi < +46\%$, and $+123\% < \psi < +57\%$ for the LA-PFHSs with the perforation sizes at 15.24 mm, 7.62 mm, and 5.08 mm, respectively. This trend can be associated with the effects of vertical flow interactions over perforations in different rows with each other, which become more significant by decreasing the size of perforations. For a better explanation, the predicted Nusselt numbers for three different perforation sizes at a given porosity of 0.15 are illustrated in Fig. 7. At a given porosity, reducing the size of perforations is equivalent to an increase in the number of perforation rows such that the heat sinks with the perforation sizes at 15.24 mm, 7.62 mm, and 5.08 mm include one, two, and threeperforation rows, respectively. Fig. 7 signifies the important effects of flow interactions over perforation rowssince $+51\% < \psi < +25\%$, $+79\% < \psi < +48\%$, and $+107\% < \psi < +69\%$ for the LA-PFHSs at the porosity of 0.15 and the perforation sizes at 15.24 mm, 7.62 mm, and 5.08 mm, respectively.

Fig. 8 illustrates the predicted Nusselt numbers of the LA-PFHSs calculated from Eq (34) while the Nusselt number of zone 3 is calculated based on the lower bound thermal performance assumption for the sections in this zone. The underpredicted Nusselt numbers indicate that the lower bound thermal performance alone is not an accurate assumption to model heat transfer in LA-PFHs, although the deviations obtained by the lower bound thermal performance are lower than those obtained by the upper bound thermal performance. Similar to the trend observed in Fig. 5, the magnitude of the upper and lower bound deviations in Fig. 8 increase by a monotonic decrease in the size of perforations (increase in the perforation rows) such that $-7\% < \psi < -31\%$, $-9\% < \psi < -36\%$, and $-11\% < \psi < -42\%$ for the LA-PFHSs with the perforation sizes at 15.24 mm, 7.62 mm, and 5.08 mm, respectively.

Thus, neither an upper bound nor a lower bound thermal performance alone is sufficiently accurate to predict the Nusselt numbers of LA-PFHSs. In the next section, the proposed model for a more accurate prediction of Nusselt numbers of LA-PFHSs is presented.

5.2. New model

Because the upper and lower bound thermal performance assumptions overpredict and underpredict the Nusselt numbers of LA-PFHSs, respectively, the accuracy of the prediction can be improved by ahybrid between the lower bound and upper bound thermal performances.Therefore, in the present study, the Nusselt number of each section in zone 3 is proposed as a linear interpolation between the upper and lower bound Nusselt numbers as follows:

$$Nu_{S,3} = \beta Nu_{LB} + (1-\beta) Nu_{UB} \quad (38)$$

where Nu_{LB} and Nu_{UB} are the Nusselt numbers of an individual section in zone 3 obtained by the lower bound and upper bound thermal performance assumptions, respectively. Also, $0 \le \beta \le 1$ is the weighting function.Certainly, the accuracy of the proposed model highly depends on the accuracy of the adopted weighting function. For finding an accurate weighting function, the key parameters affecting the thermo-fluid physics of a LA-PFHS, which are required to predict the Nusselt number of a LA-PFHS are listed as follows:

$$Nu_{\mathrm{pr,LA\text{-}PFHS}} = fn\left(\mathrm{Re}, \mathrm{Pr}, t_f, W_{\mathrm{ch}}, H, L, S_x, S_y, \phi, N_R\right) \tag{39}$$

Among the listed key variables, the first seven variables are already used to calculate Nusselt numbers of sections in zone 3. Also, since S_y is a function of N_R for a given fin height, the simplified weighting function in the present study is proposed as a function of two variables of porosity and the number of perforation rows for the entire range of porosities from 0 to 1, as follows:

$$\beta = \left(\frac{1-\phi}{1+\phi}\right)^{\frac{1}{C_1 N_R + C_2}} \tag{40}$$

where C_1 and C_2 are constants. Based on the experimental data in the present experiments, the constant values that lead to the least deviations in predicted Nusselt numbers from experimental Nusselt numbers are as follows:

$$C_1 = 0.345 \tag{41}$$

$$C_2 = 1.840 \tag{42}$$

For $\phi = 0$, the proposed model results in the average Nusselt number of the SFHS.

In addition to the deviation, the accuracy of the proposed model is described by the mean absolute error as well, described as follows [35]:

$$\mathrm{MAE} = \frac{1}{n}\sum_{i=1}^{n}\left(\frac{\left|Nu_{\mathrm{pr,LA\text{-}PFHS},i} - Nu_{\mathrm{ex},i}\right|}{Nu_{\mathrm{ex},i}} \times 100\right) \tag{43}$$

where n is the number of data.Fig. 9 illustrates the predicted Nusselt numbers ofall LA-PFHSs tested in the present experiments using the proposed model in this study.The model predicts the Nusselt numbers of LA-PFHSs with a mean absolute error of4.90%, with all the data falling within $\pm 12\%$ of the experimental Nusselt numbers.Table 2 summarizes the new model presented in this work.

The proposed model in this study is the first physics-based model in the literature to predict Nusselt numbers of LA-PFHSs. In addition, this model was developed based on the operating flow conditions and

the geometrical parameters specific to the test conditions in the present experiments. Therefore, it is necessary to assess the accuracy of this model under different geometrical parameters and flow conditions through further research. In addition, performing further detailed experimental studies are necessary in order to develop an extensive bank of experimental data. Such data would help improve the accuracy of the proposed model in this study and ultimately lead to develop a generalized model to predict Nusselt numbers of LA-PFHSs under a broad range of design parameters.

6. Conclusion

An analytical model was proposed to predict Nusselt numbers of LA-PFHSs in forced convection laminar flows based on acquired experimental data. The model showed excellent predictions of the Nusselt numbers of all LA-PFHSs tested in this study by an overall MAE of 4.90%, and all the predictions falling within $\pm 12\%$ of the experimental data. The proposed model is a hybrid between the upper and lower bound thermal performances of a LA-PFHS. It was demonstrated that using either the higher bound or the lower bound thermal performance overpredicts or underpredicts the Nusselt numbers, which indicates that a combination of boundary layer interruptions and flow interactions over perforations with each other play important role to describe physics of heat transfer in a LA-PFHS. The accuracy of weighting function for interpolation between the upper and lower bound thermal performances is crucial for accurately predicting the Nusselt numbers. The proposed weighting function in the presented model includes the effects of porosity and the vertical flow interactions between perforations in different rows. Since the proposed model is the first analytical model in the literature for predicting the Nusselt numbers of LA-PFHSs, further detailed research is required to assess the accuracy of this model under a broad range of design parameters in order to develop a generalized model for predicting Nusselt numbers of LA-PFHSs under a wide range of geometrical parameters and flow conditions.

Table 2. Summary of the proposed model in this study.

Zone 1	$N_{S,1} = 2$ $H_{S,1} = H_{ed}$ $L_{S,1} = L$ $A_{S,1} = H_{S,1} \times L_{S,1}$ $Nu_{S,1}$ is calculated from Eqs (22) to (24) by using $H_{S,1}$ and $L_{S,1}$ instead of H and L, respectively.

Zone 2

$$N_{S,2} = N_R - 1$$

$$H_{S,2} = S_y$$

$$L_{S,2} = L$$

$$A_{S,2} = H_{S,2} \times L_{S,2}$$

$Nu_{S,2}$ is calculated from Eqs (22) to (24) by using $H_{S,2}$ and $L_{S,2}$ instead of H and L, respectively.

Zone 3

$$N_{S,3} = N_R$$

$$H_{S,3} = L_P$$

$$L_{S,3} = L - \left(N_C \times L_P\right)$$

$$A_{S,3} = H_{S,3} \times L_{S,3}$$

$$L_{LB} = L - \left(N_C \times L_P\right)$$

$$L_{UB} = S_x$$

Nu_{LB} is calculated from Eqs (22) to (24) by using $H_{S,3}$ and L_{LB} instead of H and L, respectively.

Nu_{UB} is calculated from Eqs (22) to (24) by using $H_{S,3}$ and L_{UB} instead of H and L, respectively.

$$\beta = \left(\frac{1-\phi}{1+\phi}\right)^{\frac{1}{0.345 N_R + 1.840}}$$

$$Nu_{S,3} = \beta Nu_{LB} + \left(1-\beta\right) Nu_{UB}$$

Experimental Nusselt number

$$Nu_{ex} = \frac{\left(\frac{Q_{input}}{N}\right) W_{ch}}{K_f \left(2HL\right)\left(1-\phi\right)\left(T_{s,avg} - T_i\right)}$$

Predicted Nusselt number	$$Nu_{\text{pr,LA-PFHS}} = \frac{\sum_{i=1}^{3} N_{\text{S},i} A_{\text{S},i} Nu_{\text{S},i}}{\sum_{i=1}^{3} N_{\text{S},i} A_{\text{S},i}}$$

Acknowledgement

The support extended by the Office of Science in the U.S.Department of Energy, award# DE-SC0011317 is gratefully acknowledged.

Also, the authors are thankful to Ms. Abbey Gall for her support throughout the experiments.

References

[1] M.R. Shaeri, B. Richard, R. Bonner, Cooling performances of perforated-finned heat sinks, in: HT2016-7284, ASME Summer Heat Transfer Conference, Washington, DC, July 10-14, 2016.

[2] Y. Yu, T.W. Simon, M. Zhang, T. Yeom, M.T. North, T. Cui, Enhancing heat transfer in air-cooled heat sinks using piezoelectrically-driven agitators and synthetic jets, International Journal of Heat and Mass Transfer 68 (2014) 184-193.

[3] M.R. Shaeri, R. Bonner, Effect of perforation size to perforation spacing on heat transfer in laterally perforated-finned heat sinks, ASME 2017 Heat Transfer Summer Conference, Paper No. HT2017-5076, pp. V002T14A005, Bellevue, Washington, USA, July 9-12, 2017.

[4] M.R. Shaeri, T-C. Jen, The effects of perforation sizes on laminar heat transfer characteristics of an array of perforated fins, Energy Conversion and Management 64 (2012) 328-334.

[5] M.R. Shaeri, T-C. Jen, Turbulent heat transfer analysis of a three-dimensional array of perforated fins due to changes in perforation sizes, Numerical Heat Transfer, Part A 61 (2012) 807-822.

[6] A.H. Dastbelaraki, M. Yaghoubi, M.M Tavakol, A. Rahmatmand, Numerical analysis of convection heat transfer from an array of perforated fins using RANS and LES method, Applied Mathematical Modelling, In Press (2018).

[7] W. Al-Sallami, A. Al-Damook, H.M. Thompson, A numerical investigation of the thermal-hydraulic characteristics of perforated plate fin heat sinks, International Journal of Thermal Sciences 121 (2017) 266-277.

[8] M.R. Shaeri, M. Yaghoubi, K. Jafarpur, Heat transfer analysis of lateral perforated fin heat sinks, Applied Energy 86 (2009) 2019-2029.

[9] M. Yaghoubi, M.R. Shaeri, K. Jafarpur, Three-dimensional numerical laminar convection heat transfer around lateral perforated fins, Computational Thermal Sciences 1 (2009) 323-340.

[10] Md. F. Ismail, M.N. Hasan, S.C. Saha, Numerical study of turbulent fluid flow and heat transfer in lateral perforated extended surfaces, Energy 64 (2014) 632-639.
[11] A. Willockx, Using the inverse heat conduction problem and thermography for the determination of local heat transfer coefficients and fin effectiveness for longitudinal fins, Doctoral dissertation, Ghent University, 2009.
[12] K.H. Dhanawade, V.K. Sunnapwar, H.S. Dhanawade, Optimization of design parameters for lateral circular perforated fin arrays under forced convection, Heat Transfer—Asian Research 45 (2016) 30-45.
[13] K.H. Dhanawade, H.S. Dhanawade, Enhancement of forced convection heat transfer from fin arrays with circular perforation, Frontiers in Automobile and Mechanical Engineering (2010) pp. 192-196, IEEE.
[14] W.H.A.R. Al-Doori, Enhancement of natural convection heat transfer from the rectangular fins by circular perforations, International Journal of Automotive and Mechanical Engineering 4 (2011) 428-436.
[15] M.R. Shaeri, R. Bonner, Laminar forced convection heat transfer from laterally perforated-finned heat sinks, Applied Thermal Engineering 116 (2017) 406-418.
[16] M.R. Shaeri, R. Bonner, Heat transfer and pressure drop in laterally perforated-finned heat sinks across different flow regimes, International Communications in Heat and Mass Transfer 87 (2017) 220-227.
[17] N. Mohd-Ghazali, M.Z. Abu Hasan, A.S. Pamitran, S. Novianto, R. Ahmad, J.T. Oh, Investigation of compatibility of the heat transfer coefficient correlations for macro and mini channels, Energy Procedia 105 (2017) 3011-3016.
[18] S.G. Kandlikar, A general correlation for saturated two-phase flow boiling heat transfer inside horizontal and vertical tubes, Journal of Heat Transfer 112 (1990) 219-228.
[19] R. Karabacak, G. Yakar, Forced convection heat transfer and pressure drop for a horizontal cylinder with vertically attached imperforate and perforated circular fins, Energy Conversion and Management 52 (2011) 2785-2793.
[20] D.H. Lee, J.M. Jung, J.H. Ha, Y.I. Cho, Improvement of heat transfer with perforated circular holes in finned tubes of air-cooled heat exchanger, International Communications in Heat and Mass Transfer 39 (2012) 161-166.
[21] R.K. Banerjee, M. Karve, J.H. Ha, D.H. lee, Y.I. Cho, Evaluation of enhanced heat transfer within a four row finned tube array of an air cooled steam condenser, Numerical Heat Transfer, Part A 61 (2012) 735-753.
[22] X. Liu, J. Yu, G. Yan, A numerical study on the air-side heat transfer of perforated finned-tube heat exchangers with large fin pitches, International Journal of Heat and Mass Transfer 100 (2016) 199-207.

[23] M.R. Shaeri, R.W. Bonner, Lightweight and high-performance air-cooled heat sinks, IEEE, Thermal Measurement, Modeling & Management Symposium (SEMI-THERM), 2018, 34th, pp. 224-227.
[24] P. Teertstra, M.M. Yovanovich, J.R. Culham, Analytical forced convection modeling of plate fin heat sinks, Journal of Electronics Manufacturing 10 (2000) 253-261.
[25] J. Lee, I. Mudawar, Two-phase flow in high-heat-flux micro-channel heat sink for refrigeration cooling applications: Part II-heat transfer characteristics, International Journal of Heat and Mass Transfer 48 (2005) 941-955.
[26] P. Teertstra, J.R. Culham, M.M. Yovanovich, Analytical modeling of forced convection in slotted plate fin heat sinks, ASME-Publications-HTD 364 (1999) 3-12.
[27] R.J. Moffat, Describing the uncertainties in experimental results, Experimental Thermal and Fluid Science 1 (1988) 3-17.
[28] M.R. Shaeri, D. Attinger, R.W. Bonner, Vapor chambers with hydrophobic and biphilic evaporators in moderate to high heat flux applications, Applied Thermal Engineering 130 (2018) 83-92.
[29] M.R. Shaeri, D. Attinger, R. Bonner, Feasibility study of a vapor chamber with a hydrophobic evaporator substrate in high heat flux applications, International Communications in Heat and Mass Transfer 86 (2017) 199-205.
[30] M.R. Shaeri, M. Yaghoubi, Numerical analysis of turbulent convection heat transfer from an array of perforated fins, International Journal of Heat and Fluid Flow 30 (2009) 218-228.
[31] M.R. Shaeri, M. Yaghoubi, Thermal enhancement from heat sinks by using perforated fins, Energy Conversion and Management 50 (2009) 1264-1270.
[32] P. Canhoto, A.H. Reis, Optimization of forced convection heat sinks with pumping power requirements, International Journal of Heat and Mass Transfer 54 (2011) 1441-1447.
[33] S. Ndao, Y. Peles, M.K. Jensen, Multi-objective thermal design optimization and comparative analysis of electronics cooling technologies, International Journal of Heat and Mass Transfer 52 (2009) 4317-4326.
[34] M.E. Steinke, S.G. Kandlikar, Single-phase liquid friction factors in microchannels, International Journal of Thermal Sciences 45 (2006) 1073-1083.
[35] S.S. Bertsch, E.A. Groll, S.V. Garimella, A composite heat transfer correlation for saturated flow boiling in small channels, International Journal of Heat and Mass Transfer 52 (2009) 2110-2118.

Figure Caption

Fig. 1. (a) The CAD model of the experimental setup; (b) the exploded view of the experimental setup. 1: heat sink; 2: duct; 3: blower; 4 and 5: inlet and outlet RTD probes, respectively; 6 and 7: high-pressure and low-pressure sensors of the differential pressure transducer, respectively; 8: rubber gasket; 9: polycarbonate cover; 10 and 11: insulation layers.

Fig. 2. (a) The CAD model of a LA-PFHS with two rows of perforations, (b) heat sink base.

Fig. 3. Comparison of acquired experimental results for the SFHS with values calculated from widely accepted correlations in the literature. (a) pressure drops across the SFHS; (b) Nusselt numbers inside a single channel of the SFHS.

Fig. 4. Lateral side of a perforated fin with two rows and six columns of perforations, respectively, in this study.

Fig. 5. Comparison of predicted and experimental Nusselt numbers for all LA-PFHSs tested in this study, based on the upper bound thermal performance assumption in zone 3. Each perforation size covers the entire range of Reynolds numbers and porosities in the present experiments.

Fig. 6. (a) A LA-PFHS with 4 perforations, (b) flow path lines at 30% height of the LA-PFHS with 4 perforations, (c) flow path lines at 70% height of the LA-PFHS with 4 perforations, (d) a LA-PFHS with 50 perforations, (e) flow path lines at 30% height of the LA-PFHS with 50 perforations, (f) flow path lines at 70% height of the LA-PFHS with 50 perforations [9]. Reprinted from Computational Thermal Sciences, Vol. 1, M. Yaghoubi, M.R. Shaeri, K. Jafarpur, Three-dimensional numerical laminar convection heat transfer around lateral perforated fins, pp. 323-340, 2009, with permission from Begell House, Inc.

Fig. 7. Comparison of predicted and experimental Nusselt numbers for the LA-PFHSs at the porosity of 0.15. Predicted Nusselt numbers are obtained based on the upper bound thermal performance in zone 3.

Fig. 8. Comparison of predicted and experimental Nusselt numbers for all LA-PFHSs tested in this study, based on the lower bound thermal performance assumption in zone 3. Each perforation size covers the entire range of Reynolds numbers and porosities in the present experiments.

Fig. 9. Comparison of experimental Nusselt numbers of all LA-PFHSs at the entire range of tested Reynolds numbers in the present experiments with the predicted Nusselt numbers obtained by the proposed model in this study.

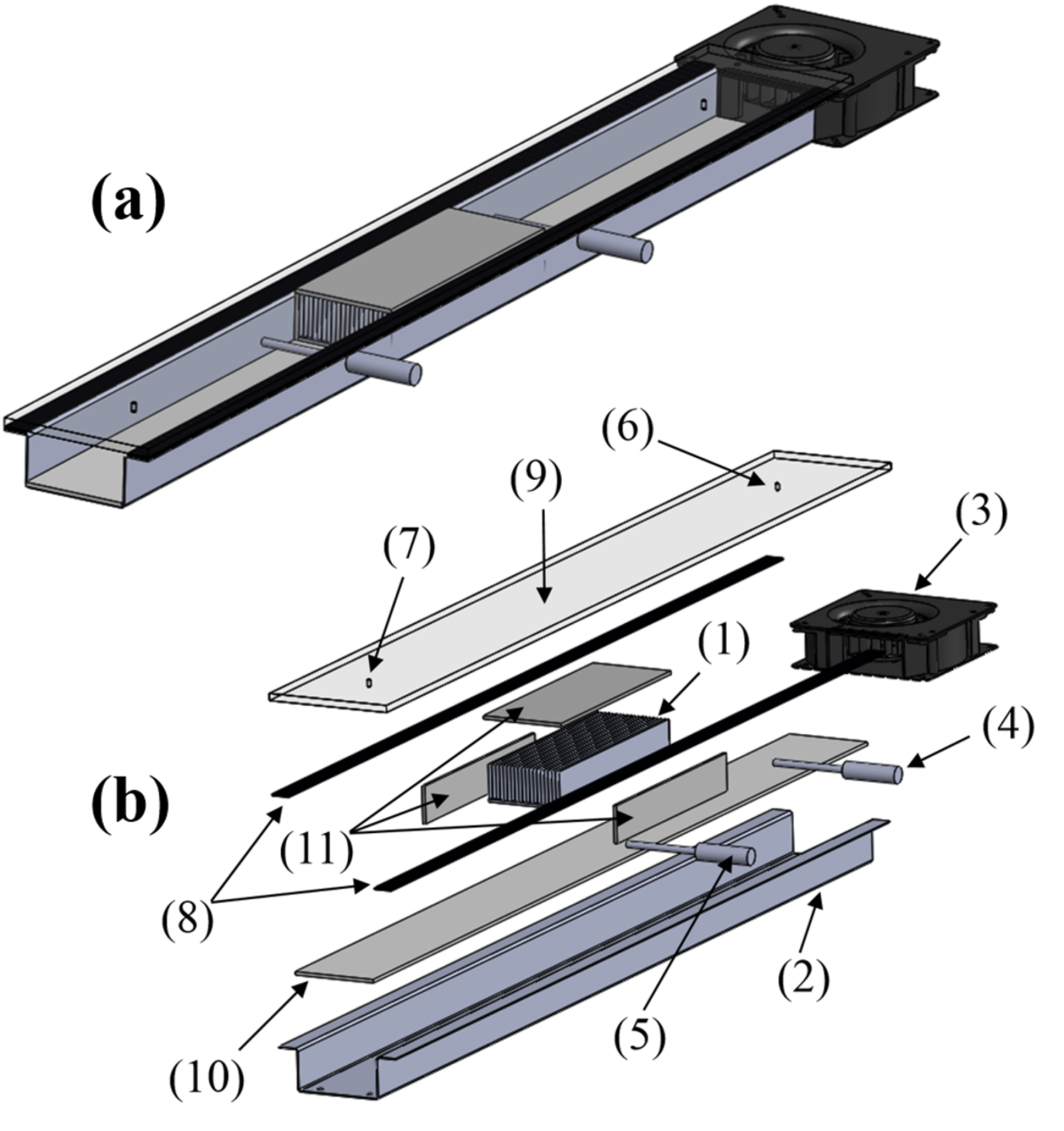
(a)
(6)
(9)
(7)
(3)
(1)
(4)
(b)
(11)
(8)
(2)
(5)
(10)

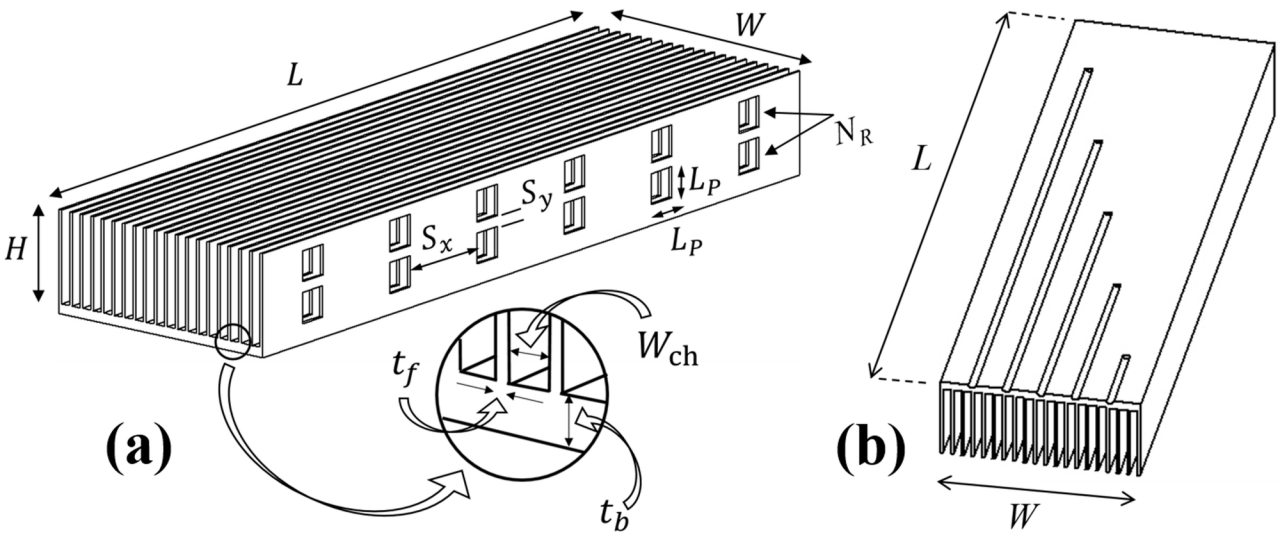
L
W
H
N_R
S_y
S_x
L_P
L_P
W_ch
t_f
t_b
(a)
L
(b)
W

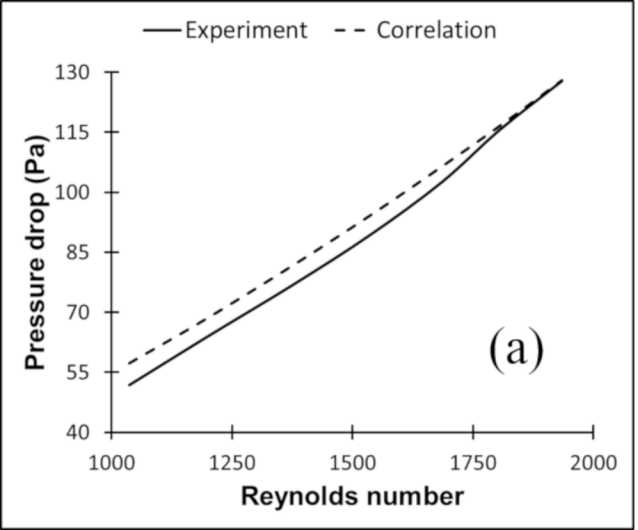
Experiment
Correlation
Pressure drop (Pa)
130
115
100
85
70
55
40
1000
1250
1500
1750
2000
Reynolds number
(a)

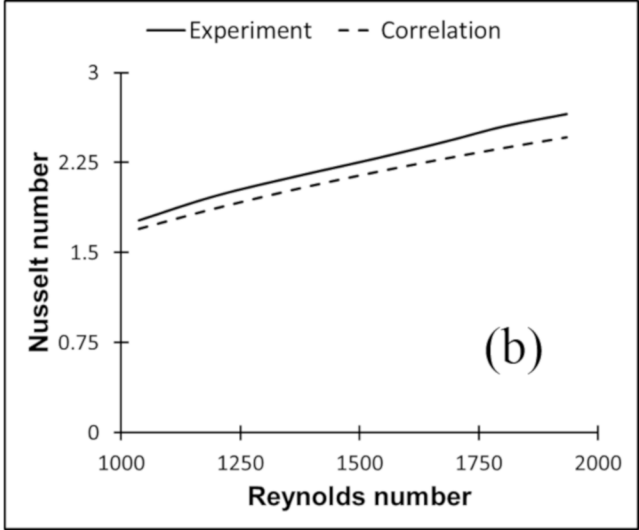
Experiment
Correlation
Nusselt number
3
2.25
1.5
0.75
0
1000
1250
1500
1750
2000
Reynolds number
(b)

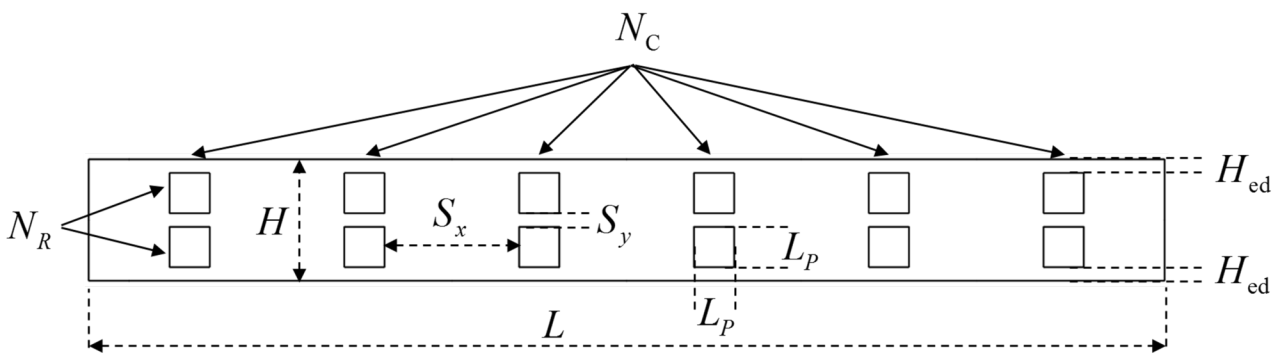
N_C
N_R
H
S_x
S_y
L_P
L_P
H_{ed}
H_{ed}
L

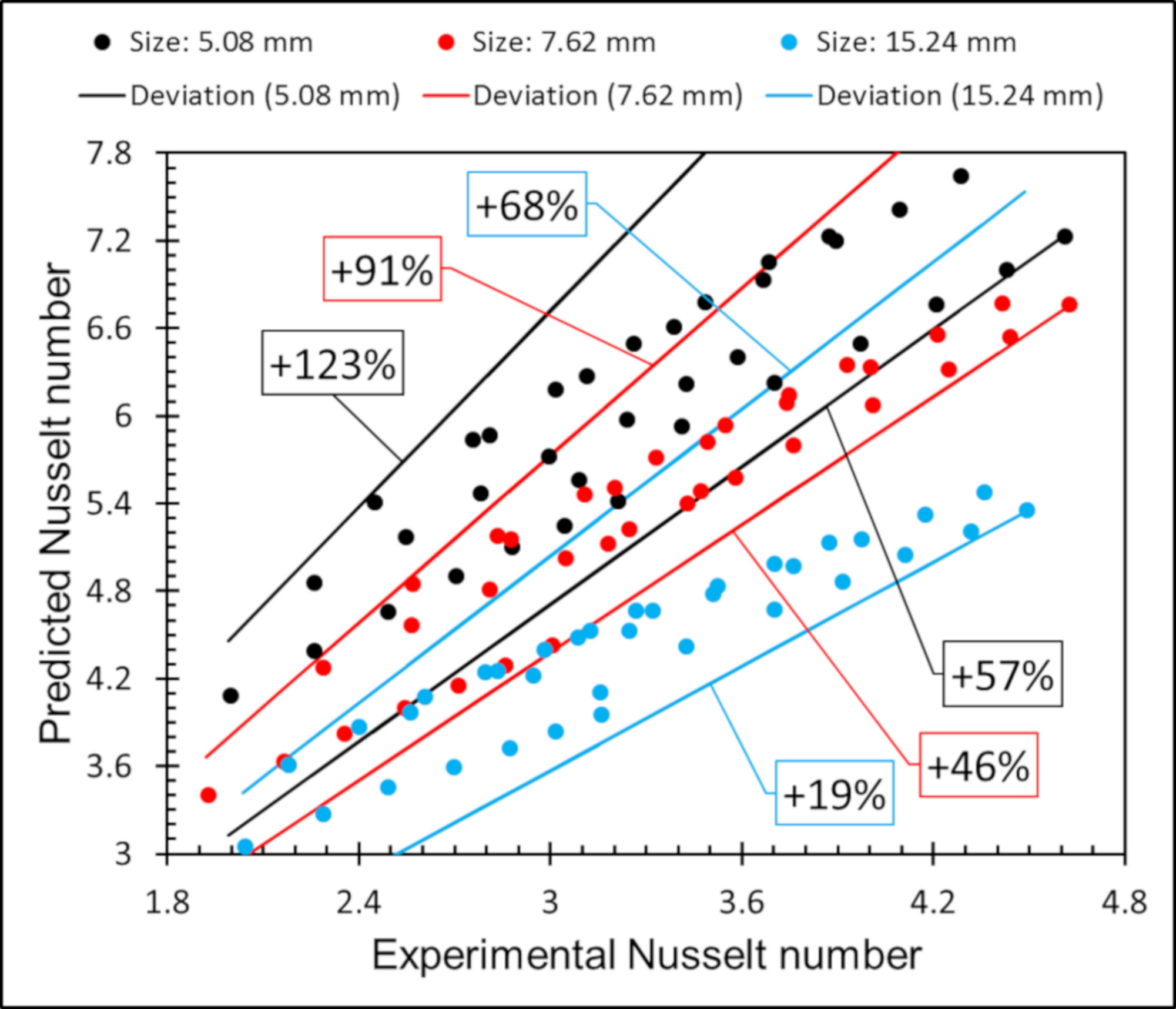
Size: 5.08 mm
Size: 7.62 mm
Size: 15.24 mm
Deviation (5.08 mm)
Deviation (7.62 mm)
Deviation (15.24 mm)
+68%
+91%
+123%
+57%
+46%
+19%
Predicted Nusselt number
Experimental Nusselt number
7.8
7.2
6.6
6
5.4
4.8
4.2
3.6
3
1.8
2.4
3
3.6
4.2
4.8

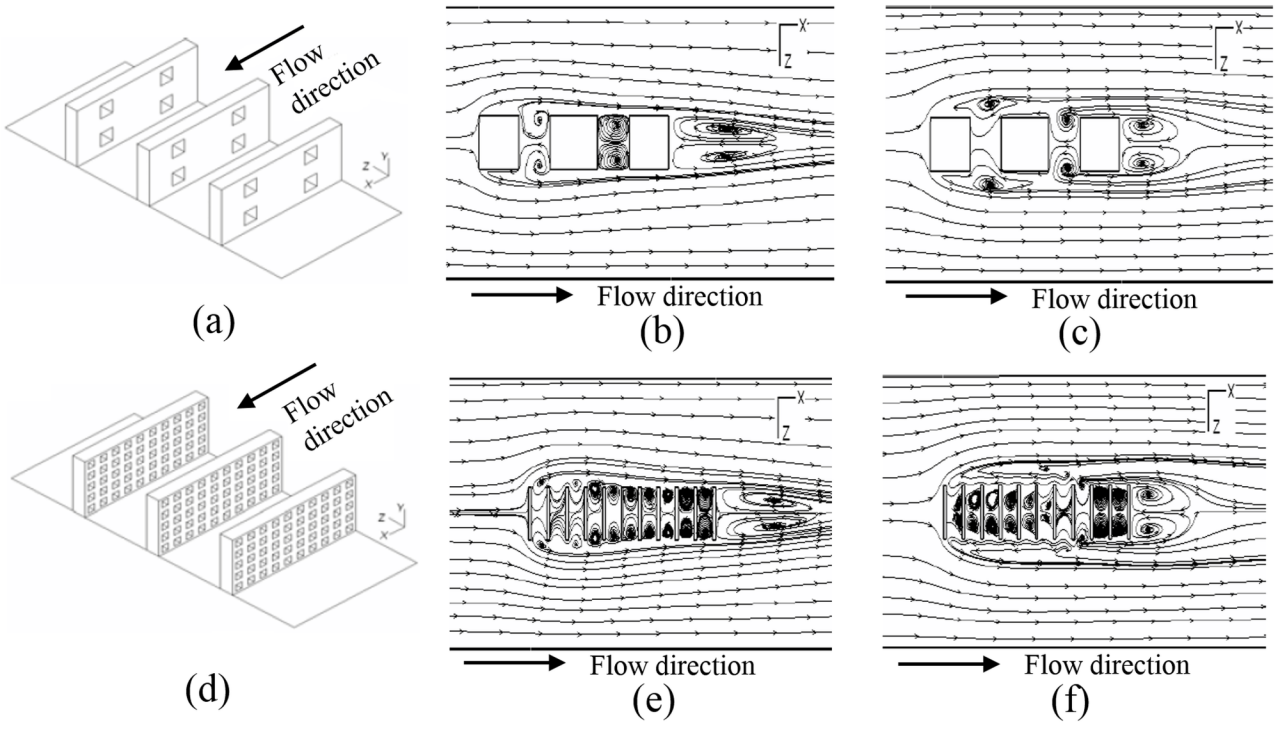
Flow direction
(a)
Flow direction
(b)
Flow direction
(c)
Flow direction
(d)
Flow direction
(e)
Flow direction
(f)

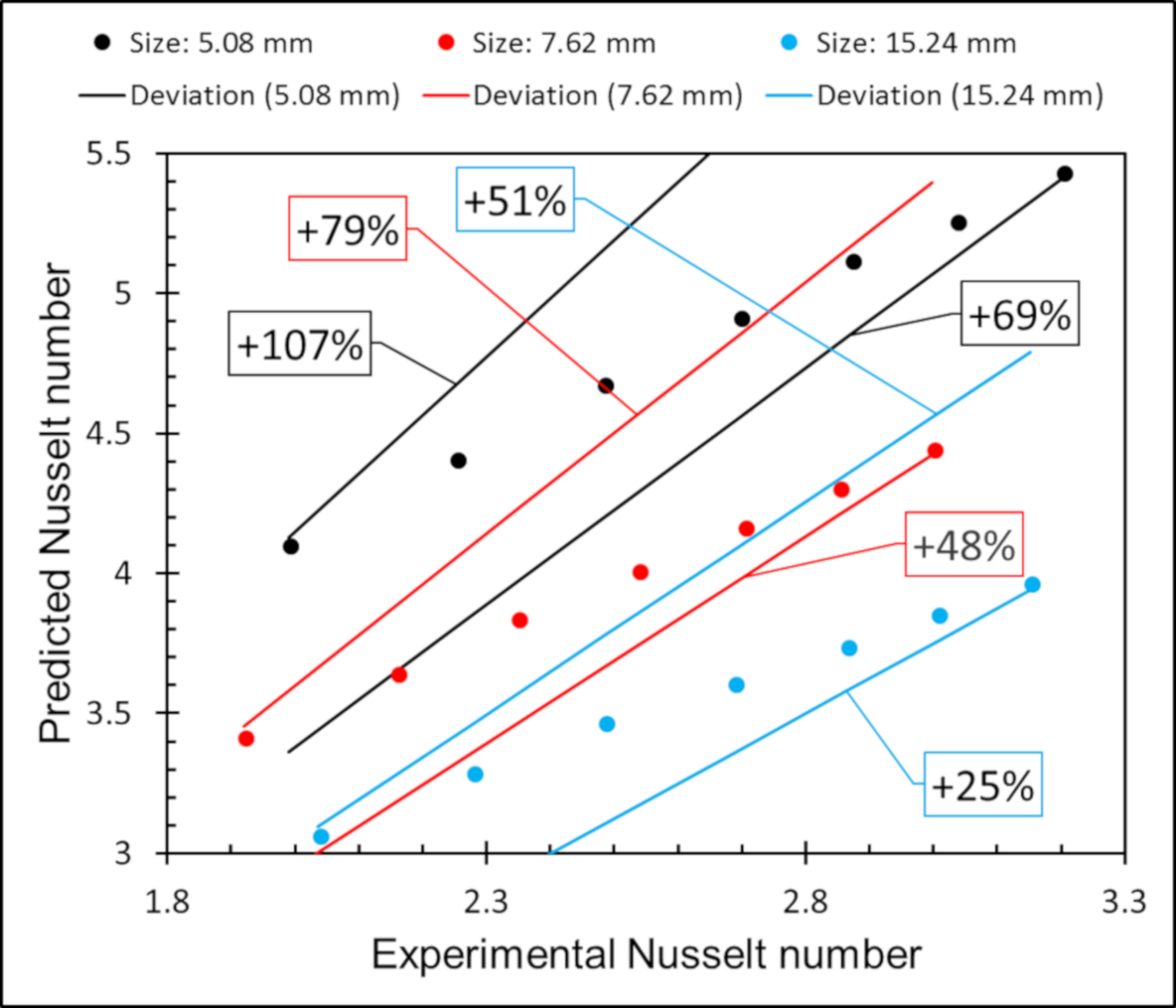
Size: 5.08 mm
Size: 7.62 mm
Size: 15.24 mm
Deviation (5.08 mm)
Deviation (7.62 mm)
Deviation (15.24 mm)
+79%
+51%
+107%
+69%
+48%
+25%
Predicted Nusselt number
Experimental Nusselt number
5.5
5
4.5
4
3.5
3
1.8
2.3
2.8
3.3

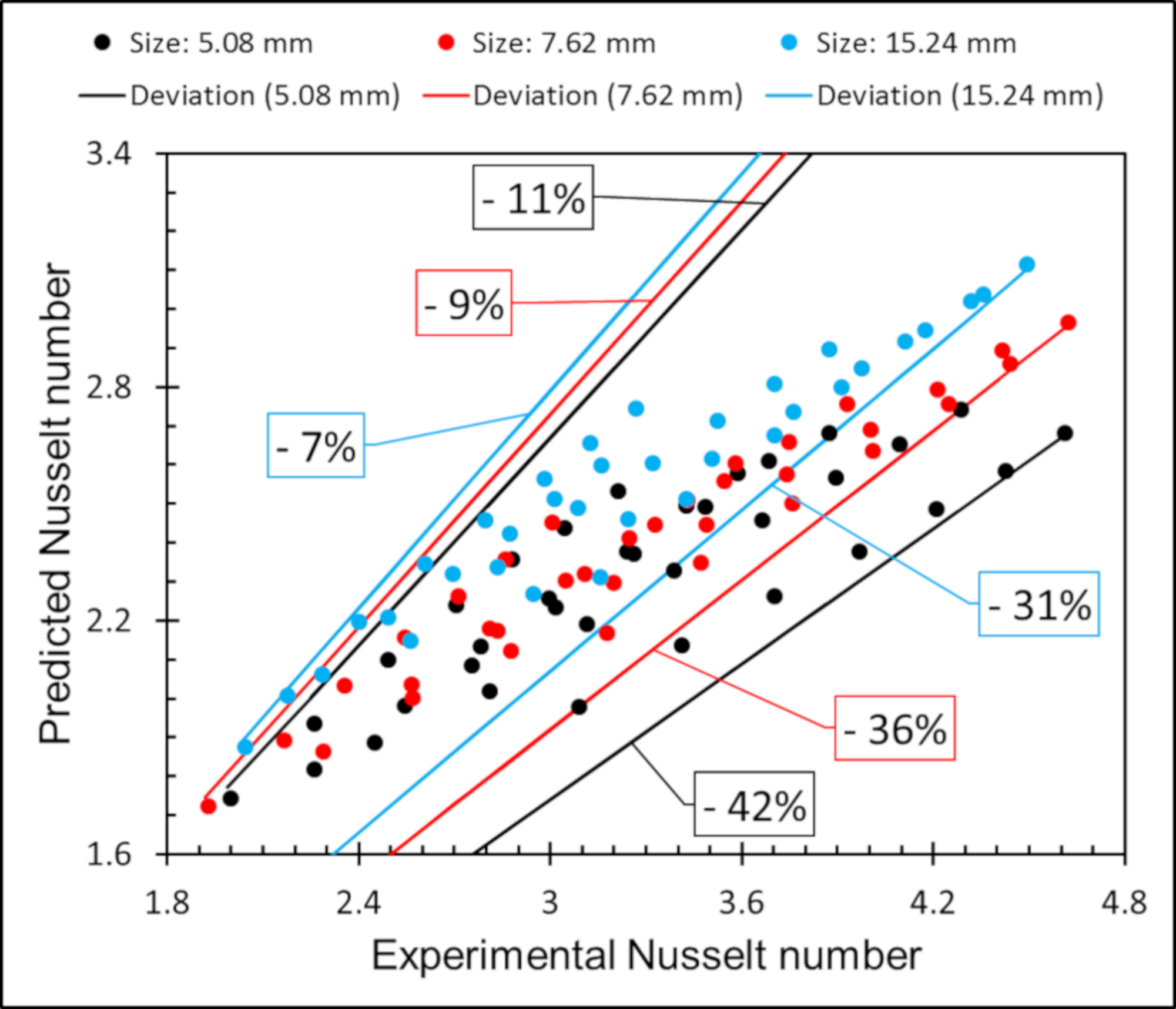
Size: 5.08 mm
Size: 7.62 mm
Size: 15.24 mm
Deviation (5.08 mm)
Deviation (7.62 mm)
Deviation (15.24 mm)
- 11%
- 9%
- 7%
- 31%
- 36%
- 42%
Predicted Nusselt number
Experimental Nusselt number
3.4
2.8
2.2
1.6
1.8
2.4
3
3.6
4.2
4.8

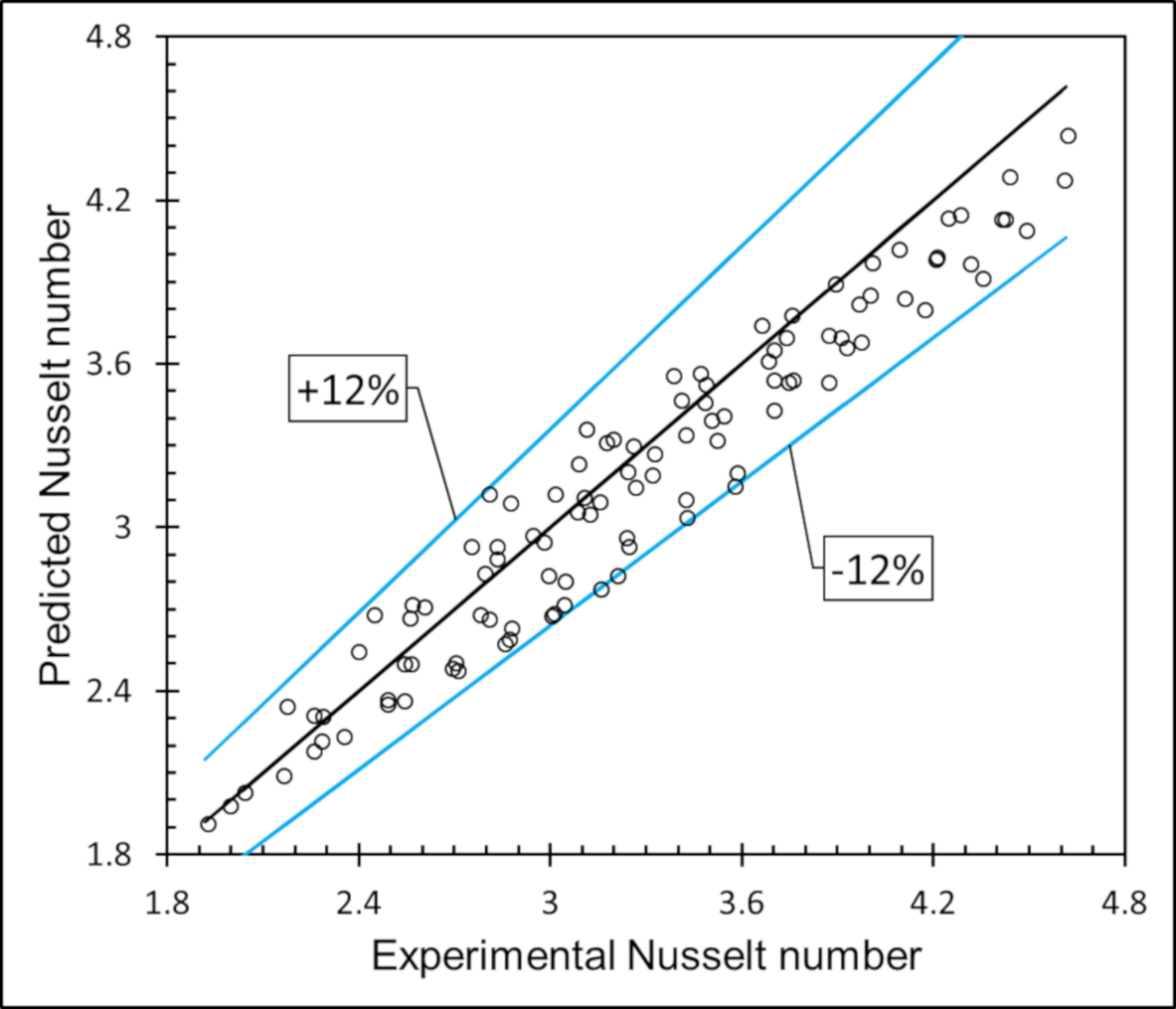
4.8
4.2
3.6
3
2.4
1.8
Predicted Nusselt number
+12%
-12%
1.8
2.4
3
3.6
4.2
4.8
Experimental Nusselt number